Solidification Behavior and Cracking Susceptibility of Pulsed-Laser Welds in Austenitic Stainless Steels

A shift in solidification behavior under rapid solidification conditions promotes an increase in cracking susceptibility

BY J. C. LIPPOLD

ABSTRACT. The solidification cracking susceptibility of several commercial heats of Types 304L, 316L and 321Mo stainless steels was evaluated under pulsed-laser welding conditions. Both the Suutala weldability diagram and the WRC constitution diagram predicted that all the heats tested in this investigation would be resistant to weld solidification cracking based on the individual values of their Cr_{eq}/Ni_{eq} ratio. Under the rapid solidification conditions imposed by pulsed-laser welding, however, a number of these "resistant" heats were found to be extremely susceptible to weld solidification cracking. As a result, a modified weldability diagram is proposed for austenitic stainless steels welded under conditions producing rapid solidification.

The variation from predicted cracking susceptibility resulted from a shift in solidification behavior under rapid solidification growth conditions. Alloys susceptible to cracking exhibited a primary austenite solidification mode with a fully austenitic microstructure. Crack-resistant alloys were also fully austenitic, but this microstructure resulted from a massive transformation to austenite following primary solidification as ferrite. Several alloys exhibited mixed solidification modes, resulting in variable cracking susceptibility. The solidification conditions under which this shift in the primary solidifying phase occurs is reviewed in the context of the current results and previous observations. The concept of a microstructural map, as a function of composition and solidification growth rate, is proposed as a means to predict the solidification behavior and associated cracking susceptibility of austenitic stainless steel welds made over a wide range of solidification conditions.

J. C. Lippold is with Edison Welding Institute, Columbus, Ohio.

Introduction

For over 50 years, the relationship between weld metal ferrite content and susceptibility to weld solidification cracking in austenitic stainless steels has been well recognized (Refs. 1–5). The general approach developed during this period has been to control the as-welded, fusion zone microstructure such that it contains 5 to 15 vol-% delta ferrite. Both field experience and laboratory testing have shown that, over a fairly broad range of composition, this level of delta ferrite is associated with weld metals that are extremely resistant to cracking. It has also been found that the quantity of weld metal ferrite was best controlled by composition rather than welding procedure and, thus, a number of constitution diagrams evolved as a means for predicting ferrite level. Most notable among these diagrams are those by Schaeffler (Ref. 2), DeLong (Ref. 3), and most recently the Welding Research Council (Refs. 4, 5).

Within the last 15 years, the relationship among weld ferrite content, solidification behavior and cracking susceptibility has been studied extensively. A unifying observation from these studies has been that it is not the absolute level of weld metal ferrite that is important with respect to cracking resistance but rather the manner in which the weld metal solidifies (Refs. 7–13). When primary solidification occurs as delta ferrite, cracking resistance is far superior to the situation when primary solidification occurs as austenite. In the former case, much of the ferrite formed during solidification transforms to austenite via a solid-state reaction that occurs on-cooling to ambient temperature. In the austenitic stainless steels, this transformation generally produces an as-welded microstructure containing from 3 to 20 vol-% delta ferrite. The variety of ferrite morphologies that have been reported in austenitic/ferritic weld metal are primarily a function of composition and the resultant ferrite content (Refs. 13–16).

When solidification occurs as austenite, the as-welded microstructure will be either fully austenitic, or contain a small amount of ferrite along solidification grain and subgrain boundaries. The level of ferrite produced under primary austenite solidification conditions is generally less than 3 vol-% in conventional austenitic stainless steels. The early development of the 5 to 15 vol-% ferrite guideline and its relationship to weld solidification cracking is thus apparent.

The weld solidification cracking susceptibility of austenitic stainless steels

KEY WORDS

Pulsed-Laser Welding
Austenitic Stainless
Solidification Cracking
Solidification Behavior
Rapid Solidification
304L Stainless Steel
316L Stainless Steel
321Mo Stainless Steel
Pred. Diag. Ferrite
Microstructure

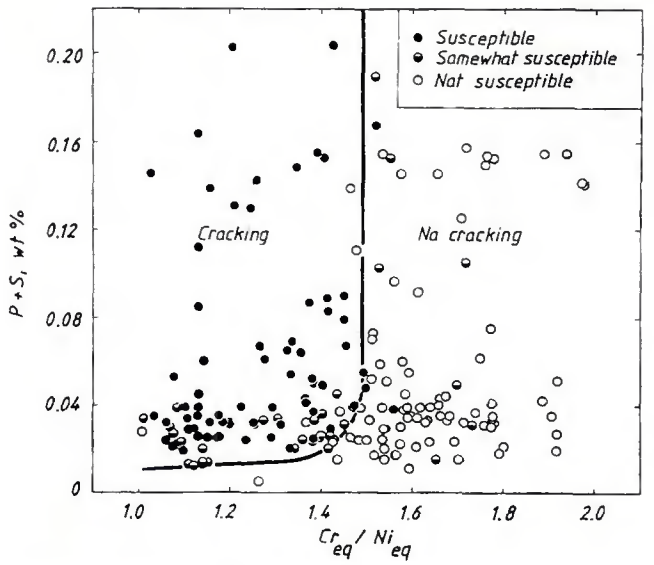

Fig. 1 — The Suutala diagram for predicting the weld solidification cracking susceptibility of austenitic stainless steels (Ref. 10).

has also been closely linked to the level of impurity elements in the weld metal. (Refs. 9, 10, 12, 13, 17, 18) The relationship between cracking susceptibility and composition, with respect to both alloy and impurity concentration, is best illustrated in the diagram devised by Suutala *et al.* (Refs. 10, 15), and shown in Fig. 1. At extremely low sulfur plus phosphorus (S + P) levels (less than 100 ppm), cracking susceptibility is low over a wide range of composition. At higher (S + P) levels, comparable to those commonly encountered in austenitic stainless steels, cracking susceptibility undergoes a sharp transition at a Cr_{eq}/Ni_{eq} ratio of 1.48. In the steels used to devise this diagram, this value of Cr_{eq}/Ni_{eq} represents the approximate transition in solidification behavior from primary austenite to primary ferrite (values greater than approximately 1.50).

It is interesting, and encouraging, to note that when delta ferrite is the primary phase of solidification, extremely high (S + P) contents can be tolerated. This diagram clearly demonstrates the efficacy of solidification control and/or reducing impurity content for preventing weld solidification cracking in austenitic stainless steels.

The Suutala diagram was devised based on weldability test data generated using conventional arc welding processes, primarily gas tungsten arc welding (GTAW). Recently, several studies involving high-energy density, low-energy input processes such as electron beam welding (EBW) and laser beam welding (LBW) have shown that the solidification behavior predicted by Suutala is inaccurate when solidification rates, and subsequent cooling rates, are extremely high (Refs. 13, 19–24). As a result, the as-welded, ambient temperature microstructure predicted by various constitution diagrams may vary significantly from that actually produced. David, *et al.* (Ref. 21), and Nakao, *et al.* (Ref. 22), have shown that the width of the austenite plus ferrite, two-phase region on the Schaeffler constitution diagram becomes progressively narrower as a function of increasing cooling rate.

The truncation of the austenite plus ferrite region at high weld cooling rates results primarily from two effects: 1) a transition from primary ferrite to primary austenite solidification in lower ferrite potential, *i.e.*, lower Cr_{eq}/Ni_{eq} alloys; and 2) the suppression of the ferrite-to-austenite transformation on-cooling in alloys with a high ferrite potential. The former effect results in either a fully austenitic structure or one with a small amount of ferrite along primary austenite solidification boundaries, while the latter results in a fully ferritic microstructure. The rapid weld cooling rates also give rise to a number of intermediate weld microstructures that are not observed when welding is performed with conventional arc welding processes. In laser surface-melted Fe-Cr-Ni alloys covering a wide range of compositions, Nakao, *et al.* (Ref. 22), has described six distinct microstructural types. These include:

1) Fully austenitic.

2) Primary austenite with eutectic ferrite.

3) Primary ferrite plus austenite.

4) Rod-like, coupled eutectic.

5) Massive austenite plus blocky ferrite.

6) Fully ferritic.

With the exception of the Type 4 structure, these microstructural types have been corroborated in various austenitic stainless steels by other inves-

Table 1 — Alloy Compositions (wt-%)

Alloy Designation[a]	ID No.	Elements Cr	Ni	Mn	Si	Mo	Ti	C	N	O	P	S	B
316L	1	16.7	12.4	1.47	0.69	2.3	—	0.020	0.026	0.006	0.02	0.006	0.0023
	2	16.6	12.0	1.67	0.66	2.2	—	0.025	0.04	0.007	0.021	0.006	0.0016
	10	16.9	11.6	1.29	0.37	2.07	—	0.02	0.037	0.008	0.024	0.021	0.0031
304L	3	18.5	10.5	1.68	0.67	—	—	0.019	0.018	0.02	0.016	0.002	0.024
	4	18.7	10.9	1.70	0.55	—	—	0.027	0.034	0.008	0.02	0.007	0.0024
	5	18.7	9.3	1.3	0.31	—	—	0.015	0.068	0.008	0.025	0.022	<0.0005
	7	18.6	10.2	1.83	0.60	—	—	0.015	0.053	0.004	0.026	0.002	0.0008
	12	18.6	10.2	1.84	0.64	—	—	0.013	0.054	0.008	0.028	0.002	0.0008
	13	18.3	9.6	1.61	0.39	—	—	0.011	0.063	0.015	0.026	0.003	<0.0005
	14	18.4	10.6	1.55	0.69	—	—	0.017	0.02	0.015	0.016	0.002	0.002
	16	18.6	9.9	1.29	0.29	—	—	0.017	0.057	0.011	0.023	0.024	0.0006
321Mo	6	17.7	11.2	1.65	0.60	0.15	0.46	0.057	0.008	0.003	0.021	<0.001	0.0019
	9	17.6	10.3	1.49	0.39	0.45	0.27	0.044	0.014	<0.002	0.02	0.002	0.0009
	11	17.5	10.1	1.50	0.35	0.24	0.38	0.044	0.011	0.004	0.021	0.02	0.0036
	15	17.3	10.2	1.50	0.49	0.30	0.46	0.047	0.011	0.027	0.023	0.022	<0.0005

(a) Alloys were obtained under the following AFNOR designations: 316L = Z2 CND 17-12, 304L = Z2 CN 18-10, 321Mo = Z6 CNDT 17-11.

tigators (Refs. 13, 14, 21, 23).

Despite the research effort devoted to investigating the effect of rapid solidification rates on the microstructure of austenitic stainless steel welds, the effect of the modification of solidification behavior on cracking susceptibility is not fully understood or widely recognized. The purpose of this study was to evaluate the cracking susceptibility of a number of commercial austenitic stainless steels welded using the pulsed-laser welding process. The laser pulse energy was adjusted to study the effect of weld shape and solidification conditions on microstructure and associated cracking susceptibility. These results were then compared to the behavior predicted using the Suutala diagram — Fig. 1. A variation to the Suutala diagram is proposed for rapid solidification conditions, such as those experienced during LBW, EBW and surface melting treatments. This investigation has also provided additional insight into the influence of rapid solidification on the solidification behavior and microstructural modification of austenitic stainless steel welds.

Materials and Procedures

The alloy designations and chemical compositions of the materials used in this study are shown in Table 1. These materials included conventional Types 304L and 316L alloys and a nominal 17Cr-11Ni alloy containing Ti and Mo (designated as Type 321Mo in this study). The Cr_{eq}/Ni_{eq} ratios of these alloys, determined using the Suutala (Ref. 10), DeLong (Ref. 3) and WRC-1992 (Ref. 5) weighting factors, are shown in Table 2. Most materials were provided in the form of round bar, with the exception of two Type 304L alloys that were in the form of tube produced via a powder metallurgy process. The welding samples prepared from round bar were sliced perpendicular to the axis of the bar with a nominal thickness of 2 mm (0.08 in.). Prior to welding the samples were thoroughly degreased.

Welding was performed using a 300-W Nd:YAG laser capable of pulse frequencies from 1 to 99 Hz and pulse durations from 0.1 to 9.9 ms. Welding conditions were adjusted to produce three penetration levels in each material, nominally 0.5, 0.8 and 1.2 mm (0.02, 0.03 and 0.05 in.). Details of the welding conditions are provided in Table 3.

After welding, samples were sectioned both transverse and longitudinal to the direction of welding. A number of sections (a minimum of three) were examined for each alloy/welding condition combination in order to provide a good estimate of cracking susceptibility. Samples were polished and etched electrolytically using a 10% oxalic acid solution. Sections were examined at magnifications up to 400X for the presence of cracks and to identify the microstructural features associated with cracking. Based on this analysis, each alloy/welding condition combination was rated as crack susceptible (cracks present in all sections), crack resistant (no cracks observed), or variable (cracking in some sections but not in others). The solidification behavior was also characterized for each section examined.

A number of metallographic sections from selected alloys were also examined using a ferro-fluid staining technique. This technique has been demonstrated to be very effective in identifying magnetic phases, such as ferrite, in stainless steels (Ref. 26).

Results

Weld Cracking Susceptibility

Weld cracking susceptibility was determined by metallographic sectioning and inspection of polished and etched samples under the optical microscope. For both the Type 316L and 304L alloys, cracking was either present or absent in all sections of a given alloy, irrespective of welding conditions. In contrast, two Type 321Mo alloys (Nos. 11 and 15) exhibited variable cracking susceptibility with some sections containing cracks and others appearing crack-free. The metallographic assessment of cracking susceptibility is summarized in Table 4 and plotted in terms of Cr_{eq}/Ni_{eq} and (S + P + B) content on a modified-Suutala diagram in Fig. 2. This diagram has been modified from the one originally proposed by Suutala (Ref. 10) by the addition of boron as an embrittling impurity element.

Table 2 — Cr_{eq}/Ni_{eq} Values

Alloy ID L	Suutala[a]	DeLong[b]	WRC-1992[c]
Type 316L			
1	1.53	1.38	1.40
2	1.51	1.34	1.37
10	1.57	1.40	1.45
Type 304L			
3	1.69	1.56	1.60
4	1.56	1.44	1.49
5	1.75	1.54	1.67
7	1.65	1.48	1.58
12	1.66	1.49	1.58
13	1.68	1.50	1.63
14	1.66	1.56	1.59
16	1.66	1.49	1.60
Type 312Mo			
6	1.54	1.44	1.43
9	1.64	1.44	1.56
11	1.66	1.55	1.59
15	1.67	1.55	1.57

(a) $\frac{Cr + 1.37Mo + 1.5Si + 2Nb + 3Ti}{Ni + 0.31Mn + 22C + 14.2N + Cu}$ (from Suutala, Ref. 10).

(b) $\frac{Cr + Mo + 1.5Si + 0.5Nb + 3Ti}{Ni + 0.5Mn + 30[C + N]}$ (Ti-factor from Suutala).

(c) $\frac{Cr + Mo + 0.7Nb + 3Ti}{Ni + 35C + 20N + 0.25Cu}$ (Ti-factor from Suutala).

Table 3 — Laser Welding Conditions

Penetration Depth (mm)	Pulse Frequency (Hz)	Pulse Length (ms)	Welding Energy (J)	Welding Speed (mm/s)
Low (0.5)	8	8	7	1.6
Medium (0.8)	8	8	12	1.6
High (1.2)	8	8	20	1.6

Focal distance = 80 mm.
Sheet thickness = 1.5 mm.

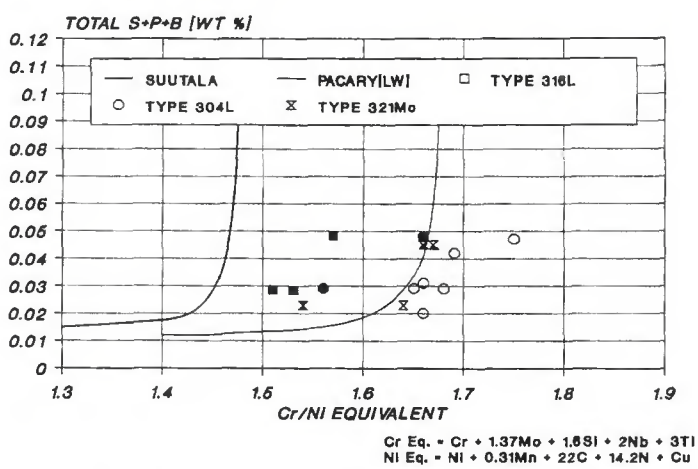

Fig. 2 — Pulsed-laser weld results plotted on the Suutala diagram. Open symbols = no cracks, filled symbols = cracks, open/filled symbols = variable cracking.

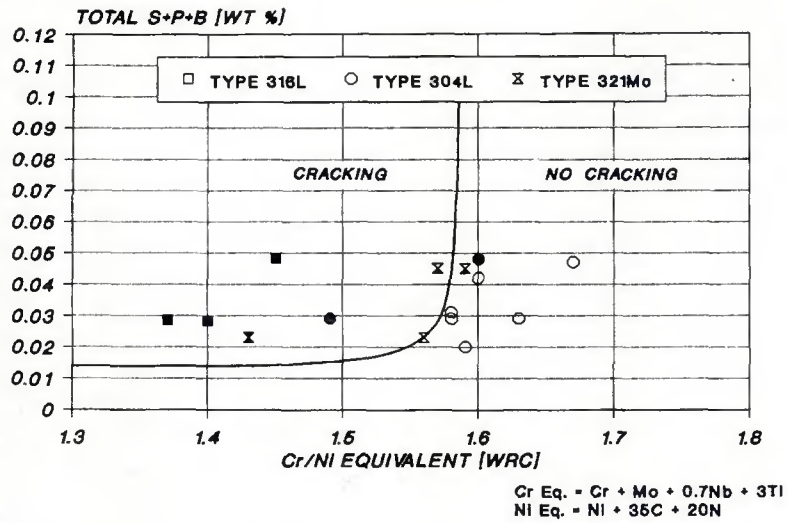

Fig. 3 — Pulsed-laser weld results plotted on modified-Suutala diagram using WRC equivalents. Open symbols = no cracks, filled symbols = cracks, open/filled symbols = variable cracking.

Note that all the alloys tested exhibited a Cr_{eq}/Ni_{eq} ratio greater than 1.48, the value originally suggested by Suutala as the demarcation of crack susceptibility. Despite this, all the alloys in the Cr_{eq}/Ni_{eq} range from 1.5 to 1.65 exhibited weld solidification cracking under pulsed-laser welding conditions. To represent this behavior, a preliminary second curve has been added to Fig. 2. This curve has been drawn to parallel the original Suutala curve with the limiting value for weld cracking resistance shifted to approximately 1.68.

Cracking susceptibility has also been plotted using the Cr_{eq}/Ni_{eq} values recently proposed by Siewert, *et al.* (Ref. 4), and Kotecki, *et al.* (Ref. 5), in the development of the WRC-1988 and WRC-1992 constitution diagrams, respectively, as shown in Fig. 3. Note that the Cr_{eq} has been modified from that originally proposed by the addition of a factor for Ti. This factor only affects the Ti-bearing Type 321Mo alloys. Titanium acts as a relatively potent ferrite-former due to its affinity for carbon and nitrogen and, thus, must be accounted for when considering ferrite formation in stainless steels. Note that a demarcation in cracking susceptibility as a function of composition and impurity content can also be developed using the WRC equivalency relationships, although one crack-susceptible Type 304L alloy (No. 16) fell in the crack-resistant region of the diagram.

In general, variation in welding conditions (via the adjustment of laser pulse energy) had little or no influence on weld solidification cracking susceptibility for a given heat of material. This is probably due to the fact that, over the range of conditions evaluated, the weld solidification behavior was not appreciably altered, as described in a following section.

Weld Metal Microstructure

In contrast to previous studies of microstructure in rapidly solidified austenitic stainless steels (Refs. 16, 22, 23), only two basic microstructural types were observed in the alloys evaluated. The first was typified by primary austenite solidification and a well-defined solidification subgrain structure. In general, no ferrite was observed in this microstructure. The second type was also fully austenitic, but appeared to result from primary ferrite solidification fol-

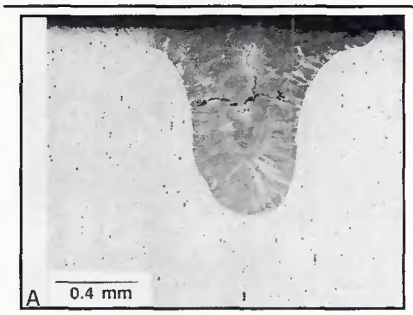

A

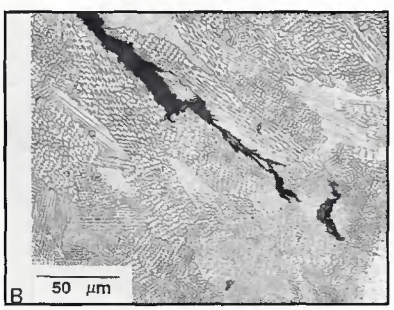

B

Fig. 4 — Primary austenite solidification mode, Type 321Mo (No. 6). A — Low magnification, 50X; B — high magnification showing cracking along solidification grain boundaries, 400X.

Table 4 — Ferrite Potential, Solidification Behavior and Cracking Susceptibility

Alloy No.	Ferrite Potential DeLong[a]	Ferrite Potential WRC[a]	Solidification Mode Predict[b]	Solidification Mode Actual[c]	Cracking (Y/N)
Type 316L					
1	2-4	0-2	AF	A	Y
2	0-2	0-2	AF	A	Y
10	2-4	2-4	FA	A	Y
Type 304L					
3	6-8	4-6	FA	A + F/MA	N
4	2-4	2-4	FA	A	Y
5	4-6	6-8	FA	F/MA	N
7	4-6	2-4	FA	F/MA	N
12	4-6	4-6	FA	F/MA	N
13	4-6	4-6	FA	A + F/MA	N
14	4-6	4-6	FA	A + F/MA	N
16	2-4	4-6	FA	A + F/MA	Y
Type 321Mo					
6	4-6	0-2	AF/FA	A	Y
9	4-6	2-4	FA	F/MA	N
11	4-6	4-6	FA	A + F/MA	V (4)
15	6-8	4-6	FA	A + F/MA	V (4)

(a) Ferrite Potential in terms of Ferrite Number (FN).
(b) Predicted from work of Suutala (Ref. 10).
A = primary austenite, AF = primary austenite with eutectic ferrite.
FA = primary ferrite with peritectic/eutectic austenite, F = primary ferrite.
(c) All welds were fully austenitic.
A = primary austenite, F/MA = primary ferrite/massive transformation to austenite, A + F/MA = mixed solidification mode, primary and massive austenite.
(d) Variable (V), cracking observed in "A" regions.

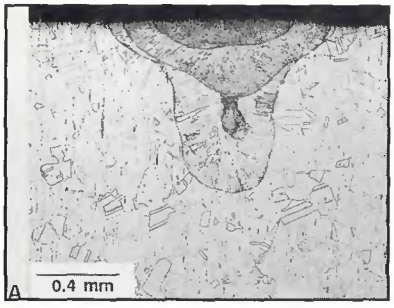

A

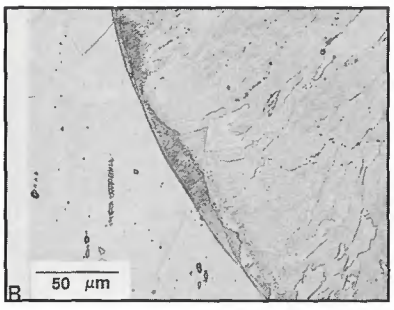

B

Fig. 5 — Primary ferrite solidification mode, Type 304L (No. 5). A — Low magnification, 50X; B — high magnification of a region near the fusion line representative of transformation to austenite, 400X.

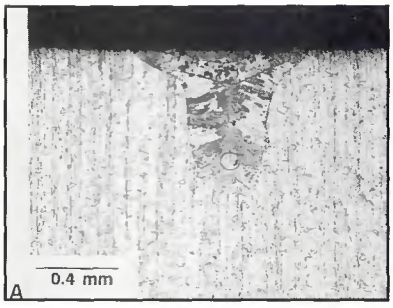

A

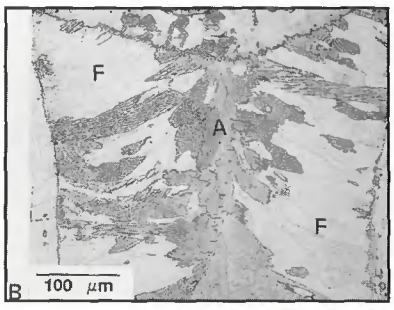

B

Fig. 6 — Mixed mode solidification, Type 321Mo (No. 11). A — Low magnification, 50X; B — adjacent regions of primary austenite (A) and primary ferrite (F) solidification, 200X.

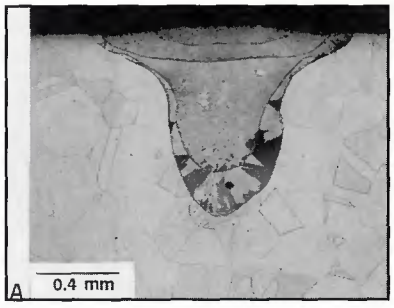

A

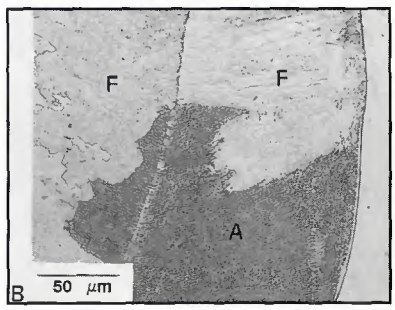

B

Fig. 7 — Mixed mode solidification, Type 304L (No. 3). A — Low magnification, 50X; B — region near weld fusion boundary, 400X.

lowed by a solid-state massive transformation to austenite, as described by previous investigators (Refs. 13, 22–25). The ferrite appeared to be completely transformed, and the solidification substructure was much less distinct than when solidification occurred as primary austenite. Many of the alloys exhibited a mixture of these two microstructures. A summary of the microstructural observations are provided in Table 4.

A cross-section of a representative alloy that solidified as primary austenite is shown in Fig. 4A. Note that the solidification cracks are large relative to the weld dimensions and occur preferentially along weld solidification grain boundaries. This is illustrated in a higher magnification micrograph of the weld metal microstructure in Fig. 4B.

A representative cross-section of an alloy that solidified as primary ferrite is shown in Fig. 5A. As in the weld shown in Fig. 4A, the weld microstructure is fully austenitic. Note, however, that the etching characteristics of this structure are distinctly different and that the boundaries between individual laser pulses are more evident relative to Fig. 4A. At higher magnification (Fig. 5B), it can be seen that the weld substructure boundaries are relatively indistinct, indicative of solidification as ferrite (Refs. 13, 15, 25). Typically, no residual ferrite was observed in welds of this type; the original primary ferrite was completely consumed by a solid-state transformation to austenite. To verify that the structure shown in Fig. 5 was austenitic, rather than retained ferrite, a ferro-fluid staining technique was used (Ref. 26). This technique is extremely effective in identifying ferromagnetic phases, such as ferrite, in both austenitic and duplex stainless steels. The use of this technique on metallographically prepared welds from alloys 5, 7, 12 and 9 (Tables 1 and 4) revealed that the microstructures were nonmagnetic and, presumably, consisted of austenite resulting from a massive transformation.

The combination of rapid diffusion in the ferrite relative to austenite and the complete transformation of the ferrite tends to mask any evidence of the original solidification structure. This observation is consistent with that reported previously (Refs. 14, 15, 25). Solidification cracking was not observed in welds in which the microstructure shown in Fig. 5 was predominant.

Several of the alloys exhibited a mixed microstructure, containing regions of both primary and transformed austenite (see Table 4). A low magnification cross-section of one of these welds in a Type 321Mo alloy is shown in Figure 6A. Solidification cracking, when present in these welds, was associated with the dark-etching regions of the weld representative of primary austenite solidification. The light-etching regions, representative of solidification as primary ferrite and transformation to austenite, were crack-free. At higher magnification in Fig. 6B, the distinct difference in solidification behavior is apparent on a microstructural scale. The adjacent regions of the microstructure that solidified as either primary ferrite or primary austenite are similar to the microstructures shown previously in Figs. 4B and 5B, respectively. These adjacent regions were crystallographically distinct as evidenced by the difference in solidification growth direction across the boundary.

The relative proportion of microstructure that solidified as either primary ferrite or primary austenite in a mixed-mode weld varied significantly among the alloys evaluated. Figure 7 shows a weld in Type 304L (alloy No. 3) that solidified predominantly as primary ferrite, but contains distinct regions in the root of the weld resulting from primary austenite solidification. In contrast to the weld shown previously, the mixed-mode weld in Fig. 7 did not exhibit cracking, indicating that as the proportion of primary ferrite solidification increases the cracking susceptibility decreases.

Heat-affected zone (HAZ) liquation cracking was observed in both the 316L and 321Mo welds. Representative sections, shown in Fig. 8, suggest that cracking in the HAZ probably resulted from propagation of weld solidification cracks across the fusion boundary. A small shift

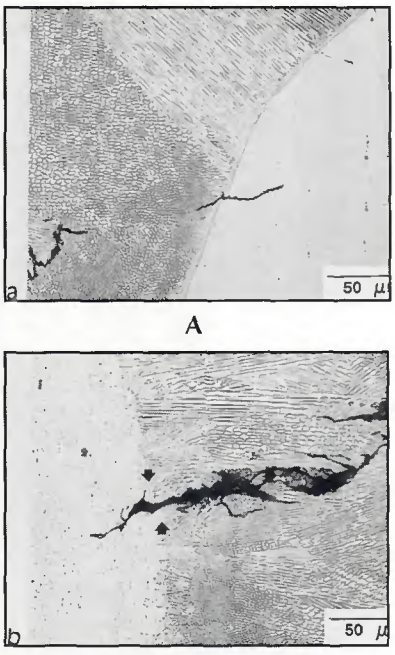

Fig. 8 — HAZ liquation cracking, 400X. A — Type 316L (No. 2); B — Type 321Mo (No. 6). Note shift in fusion boundary across crack.

in the fusion boundary was often observed across these cracks, suggesting that some grain boundary sliding occurs as a result of deformation and crack propagation along liquated grain boundaries. HAZ liquation cracking was not observed in the absence of fusion zone cracking. HAZ cracks were observed in crack-susceptible heats of Type 316L and 321Mo, but were absent in the two Type 304L alloys that exhibited weld solidification cracking. The presence of these cracks is somewhat surprising considering the low weld energy inputs and the resulting steep temperature gradients generated in the HAZ.

Effect of Welding Conditions

Variation of the welding conditions, accomplished by adjusting the laser pulse energy, altered the weld penetration and depth/width ratio but had little influence on weld solidification conditions or microstructure within a given heat. One of the 321Mo alloys (No. 11) exhibited a shift from a mixed solidification mode to a fully austenitic mode with increased penetration (highest power level). This shift was accompanied by an increased susceptibility to weld solidification cracking.

Over the range of welding conditions evaluated, composition was found to be more important than weld heat input in controlling the weld microstructure. This suggests that the variation in weld energy input over this parametric range had little influence on the solidification conditions. Little difference in primary dendrite arm spacing was observed among welds made at the three pulse energy levels, suggesting that the effective cooling rate experienced by these welds was nearly equivalent.

Discussion

The results of pulsed-laser welding and subsequent metallurgical evaluation of Type 304L, Type 316L and Type 321Mo stainless steels have revealed that the weld microstructure and solidification cracking susceptibility of these welds vary considerably from that predicted by the WRC and Suutala equivalency relationships, respectively (Table 4). This behavior has serious implications regarding the use of these relationships in applications where pulsed-laser welding and/or other processes that produce rapid solidification rates are required. Considering the importance of austenitic stainless steels in a variety of applications requiring these processes, it becomes important to both understand the mechanism by which this deviation from expected behavior occurs and develop a means to better predict their cracking susceptibility.

Prediction of Cracking Susceptibility Equivalency Relationships

Equivalency relationships, such as those proposed by DeLong (Ref. 3), WRC (Refs. 4, 5) and Suutala (Ref. 10), simplify the compositional treatment of austenitic stainless steels by providing a single value to describe the ferrite- and austenite-forming potency of a given alloy in terms of Cr_{eq} and Ni_{eq}, respectively. In addition, the ratio of these two values can be used to predict solidification behavior and subsequent cracking susceptibility in austenitic stainless steel welds made using a variety of arc welding processes. As shown in Figs. 2 and 3, the use of these ratios is also effective in differentiating cracking susceptibility in welds that solidify under more extreme conditions.

Based on the results of this investigation, a slightly better correlation between cracking susceptibility and Cr_{eq}/Ni_{eq} was obtained using the Suutala equivalents. The cracking/no cracking transition region was somewhat smaller using this ratio, relative to that of WRC. In addition, one heat of Type 304L (No. 16), which was susceptible to solidification cracking, fell within the crack-resistant envelope defined by the other alloys using WRC equivalents. In general, the correlation using both equivalency relationships was good. It is expected that the location of the cracking/no cracking transition will shift slightly as additional alloys are tested. However, a sharp transition is probably not attainable since an inherent "diffuseness" of this transition region exists due to subtle alloy-to-alloy differences, and the nature and level of the restraint, which promotes the cracking. Thus, some caution should be exercised in using the diagrams in Figs. 2 and 3. Under rapid weld solidification conditions, alloys with a Cr_{eq}/Ni_{eq} exceeding 1.7 in Fig. 2 (Suutala equivalents) and 1.65 in Fig. 3 (WRC equivalents) would be expected to be resistant to cracking.

Impurity Effects

The influence of impurity concentration cannot be neglected in any treatment of weld solidification cracking. The Suutala diagram (Fig. 1) clearly demonstrates the capacity of primary ferrite solidification in mitigating the influence of impurity segregation and, conversely, the extreme sensitivity of welds that solidify as primary austenite to the presence of impurity elements. The precise mechanism by which these impurities act to embrittle welds in the solidification range is still unclear, but a preponderance of evidence suggests that segregation of elements such as phosphorus, sulfur and boron to solidification grain and subgrain boundaries aids in depressing the local solidification temperature and promoting the formation of liquid films. These films may persist to temperatures well below the bulk solidus temperature and, if they are capable of effectively wetting a large fraction of the boundary, act to embrittle the weld under the imposition of sufficient restraint.

Irrespective of the precise mechanism, it is clear that the presence of impurities, even in small concentrations, is extremely damaging in alloys that solidify as austenite. The original Suutala diagram (Fig. 1) suggests that only at (P + S) levels below 100 ppm can cracking be avoided, irrespective of bulk composition. In practice, such levels are difficult to achieve and, when present, often create problems with respect to weld penetration. As a result, an approach based on control of the alloy bulk composition is more practical for controlling weld solidification.

The composition-based, predictive diagrams presented in Figs. 2, 3, 9 and 10 represent Suutala-type diagrams that have been modified by the addition of boron as an impurity element. The deleterious effects of boron on weld solidification cracking susceptibility in stainless steels and nickel-based alloys has been reported (Refs. 27–29). During single phase solidification as austenite, this element has a similar behavior to phospho-

rus and sulfur in partitioning to weld solidification boundaries where it is effective in locally depressing the solidification temperature and aiding in the wetting ability of liquid films (Ref. 30). Although normally present in small concentrations in austenitic stainless steels, as evidenced by the alloys evaluated in this investigation, its presence is potentially damaging and thus is included to alert the readers to this danger.

The (S + P + B) factor is presented as a simple sum, although it may be more appropriate to assign weighting factors to these elements in a manner similar to the equivalency factors. Unfortunately, the individual effects of impurity elements have never been quantified using any systematic approach.

Work by Katayama, *et al.* (Ref. 16), has suggested that phosphorus is more detrimental than sulfur with respect to cracking during primary austenite solidification, but there are insufficient data on which to develop a relative weighting factor. Again, the most practical approach with respect to insuring cracking resistance appears to be through the control of bulk weld metal composition.

Solidification Behavior

Reference to Table 4 indicates that predicted vs. actual weld solidification behavior can vary considerably when using pulsed-laser welding and that this deviation significantly influences cracking susceptibility. This relationship is clearly demonstrated by superimposing the observed solidification mode on the modified-Suutala diagram, as shown in Figs. 9 and 10. Note that all the alloys that lie within the crack-susceptible region of the diagrams solidified as either primary austenite or via a mixed mode.

The cracking susceptibility of alloys that underwent mixed mode solidification was variable and appeared to be alloy dependent. Several Type 304L alloys (Nos. 3, 13 and 14) that solidified in a mixed mode solidification were resistant to cracking, while Type 321Mo alloys (Nos. 11 and 15) typically exhibited cracking in the regions that solidified as primary austenite. This is in part due to the relative proportions of microstructure arising from the alternate modes of solidification and also to the higher impurity levels in the crack-susceptible alloys.

Reference to Tables 2 and 4, and Figs. 9 and 10 also reveals that the relationship between solidification behavior and composition is not entirely straightforward. Based on the limited alloy data presented in this study, it appears that a transition from primary austenite to primary ferrite solidification for similar rapid solidification conditions occurs between 1.6 to 1.7 using the Suutala Cr_{eq}/Ni_{eq} ratio, and 1.55 to 1.65 using the WRC equivalents. The absolute position and width of this transition region is undoubtedly dependent on solidification conditions and may also be influenced by alloy type. For example, individual alloys with the same Cr_{eq}/Ni_{eq} values but varying in constitution with respect to Mo, Ti, Nb, etc. may solidify differently under identical welding conditions.

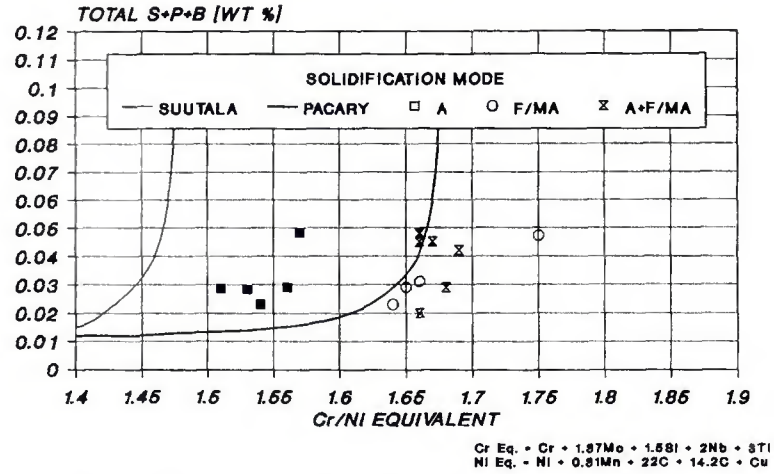

Fig. 9 — Modified-Suutala diagram with solidification mode superimposed. Filled symbols = cracking, open symbols = no cracking, filled/open symbols = variable.

Shift in Solidification Mode

Under normal weld solidification conditions, the solidification mode in austenitic stainless steels is primarily a function of composition, with a shift from primary ferrite to primary austenite accomplished by reducing the Cr_{eq}/Ni_{eq} value below some critical value. Suutala, et al. (Ref. 10), proposed that this critical ratio was approximately 1.50. Based on the results of this investigation and those of other investigators (Refs. 20–25) for alloys in the Cr_{eq}/Ni_{eq} range from 1.50 to 1.65, it is possible to effect a similar shift in solidification mode by appropriately altering the solidification conditions such that solidification is extremely rapid. The transition from primary ferrite to primary austenite under pulsed-laser welding conditions observed in this investigation and under EBW conditions (Refs. 23, 31), laser surfacing (Ref. 22) and by splat-cooling (Ref. 32), is the direct result of the rapid solidification growth rates and high cooling rates associated with these processes.

In an effort to explain this behavior, David, *et al.* (Ref. 21), and Vitek, *et al.* (Ref. 32), have suggested that the shift in solidification mode is controlled by the magnitude of weld pool undercooling below the alloy liquidus temperature. For alloys that solidify as primary ferrite

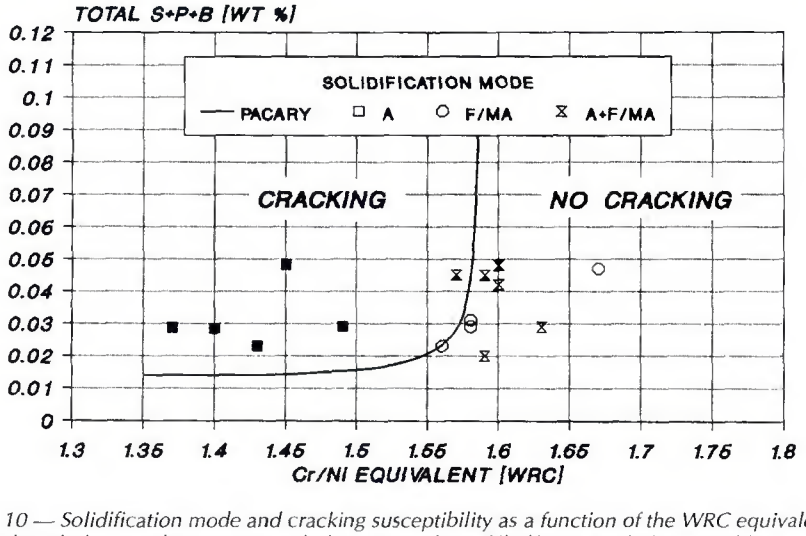

Fig. 10 — Solidification mode and cracking susceptibility as a function of the WRC equivalents. Filled symbols = cracking, open symbols = no cracking, filled/open symbols = variable.

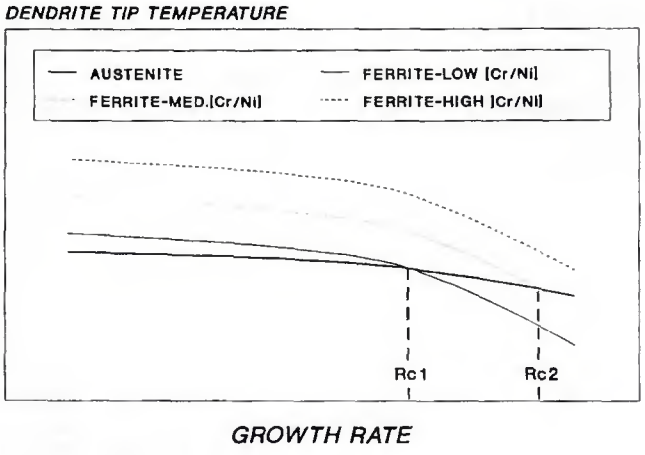

Fig. 11 — Schematic representation of the effect of solidification growth rate on dendrite tip temperature for ferrite and austenite.

under normal weld cooling conditions, their model proposes that extremely rapid cooling effects a shift in solidification to primary austenite due to liquid undercooling below some critical temperature. Undercoolings on the order of 50 K are proposed to support this model (Ref. 32).

This model has two drawbacks in explaining the observed shift in solidification from primary ferrite to primary austenite. First, since the critical temperature below which the molten pool must be cooled to promote a shift is defined as the partitionless solidification temperature, the model assumes that there is little or no solute segregation associated with austenite solidification. Based on the etching response of the microstructure shown in Fig. 4B, it is evident that solute and/or impurity partitioning is significant and, in fact, sufficient to promote solidification cracking along solidification grain boundaries. Second, it is unlikely that undercoolings of the magnitudes required by this model are achievable in the weld pool. With numerous heterogeneous nucleation sites available due to the epitaxial nature of weld solidification from a base metal substrate, suppressing nucleation over more than a few degrees below the liquidus at any location in the weld pool would be difficult (Refs. 32, 33). The magnitude of undercooling proposed is achievable when nucleation is more difficult, such as during rapid solidification of metallic powders, but seems unlikely in the presence of abundant nucleation sites, such as are present in a typical fusion weld.

The concept of local undercooling at the solid-liquid interface, as originally proposed by Suutala (Ref. 35), is more appropriate for explaining the shift in solidification behavior. This undercooling is a function of the dendrite tip radius and, thus, as solidification growth velocity increases (tip radius decreases) the local undercooling of the dendrite tip also increases. (Refs. 36, 37) The magnitude of this undercooling, as proposed by Burden and Hunt (Ref. 36), can be expressed as:

$$T_d = T_L - GD/R - CR^{0.5} \quad (1)$$

where, T_d is the dendrite tip temperature, T_L is the alloy liquidus temperature, G the temperature gradient in the liquid, D the diffusivity, R the solidification growth rate, and C a physical constant relating the Gibbs-Thomson parameter, liquidus slope, distribution coefficient and liquid diffusivity. The net undercooling is therefore $T_L - T_d$. Brooks, *et al.* (Ref. 13, 25), has previously demonstrated the importance of dendrite tip undercooling on microsegregation.

In the case of austenitic stainless steels, local undercooling can influence both segregation and solidification mode. Suutala (Ref. 35) has proposed that at high solidification growth rates, sufficient dendrite tip undercooling occurs to promote a shift in solidification mode from primary ferrite to primary austenite. This shift is dependent on both composition and growth rate, with a critical growth rate existing for a given composition to allow this transition. This concept is illustrated schematically in Fig. 11, by plotting the dendrite tip temperature vs. growth rate for alloys of varying Cr_{eq}/Ni_{eq}. The preferred primary phase of solidification will be that with the highest dendrite tip temperature at a given growth rate. Although the physical constants comprising C in Equation 1 are not well defined, Suutala (Ref. 35) and others (Refs. 38, 39) have proposed that this constant changes more rapidly for ferrite than austenite as a function of growth rate. As a result, the dendrite tip temperature of the ferrite drops more rapidly than austenite as a function of growth rate and, at a critical growth rate, may intercept the curve for austenite. Above this critical growth rate, primary austenite solidificaton predominates over primary ferrite solidification. The value of this critical growth rate is composition-dependent, increasing with higher Cr_{eq}/Ni_{eq}, as illustrated by the low and medium Cr_{eq}/Ni_{eq} values in Fig. 11.

Extrapolating the behavior predicted in Fig. 11 to the present work, alloys with a Cr_{eq}/Ni_{eq} equivalent in the range from 1.5 to 1.6 (Suutala equivalents from Figs. 2 and 9) can be approximated by the low Cr_{eq}/Ni_{eq} curve. Thus, above a critical growth rate, R_{c1}, primary austenite solidification is preferred in low Cr_{eq}/Ni_{eq} alloys. In medium Cr_{eq}/Ni_{eq} alloys, perhaps in the range from 1.65 to 1.75 primary ferrite solidification is favored at R_{c1} and does not become unfavorable until some higher critical growth rate, R_{c2}, is exceeded. Between R_{c1} and R_{c2}, sufficiently rapid cooling following solidification may promote a massive transformation to austenite, thus rendering the structure either fully or partially austenitic (Ref. 22–24). In the high Cr_{eq}/Ni_{eq} case, sufficient undercooling cannot be achieved to promote a shift in solidification behavior. These alloys may also effectively resist a solid-state transformation to austenite and exhibit ferritic microstructures.

Growth Orientation Effects

The presence of mixed mode solidification in several alloys may be rationalized, in theory, by the local variation in growth rate that is characteristic of fusion welds. The absolute growth rate in the fusion zone varies as a function of crystallographic orientation relative to the instantaneous solid-liquid interface. The upper limit of growth rate, the actual welding speed, is only achieved by grains growing normal to the solid-liquid interface at the centerline of the weld. Other grains will grow at some fraction of this speed along preferred growth directions (<100> in FCC and BCC materials), until they are eliminated via competitive growth. As a result, adjacent grains can experience significantly different growth velocities. This variation may explain the mixed mode solidification structures that were observed in some of the pulsed-laser welds — Figs. 6 and 7.

The difference in growth direction between adjacent regions that solidified as ferrite and austenite is evident in Fig. 12.

In the regions that solidified as austenite, growth appears to be primarily in the plane of the photomicrograph, while the adjacent region that solidified as ferrite exhibits a growth orientation normal to this plane (the primary ferrite subgrain structure is relatively indistinct, even after extended etching). Assuming that the weld solidification front moved primarily from left to right in Fig. 12, the grain which solidified as austenite would have been more favorably oriented along the macroscopic solid-liquid interface and, thus, would have solidified at a higher growth velocity. The complex nature of macroscopic weld solidification in pulsed-laser welds makes it difficult to estimate the difference in solidification growth direction and, hence, the rate between adjacent grains. More carefully designed experiments are necessary to quantify these differences.

In a previous investigation (Ref. 31), a transition in solidification mode from ferrite to austenite along the centerline of electron beam welds in Type 304L was attributed to the development of a solidification growth front whose velocity was equivalent to the welding speed. This resulted in a fully austenitic region at the centerline that was susceptible to solidification cracking. The surrounding microstructure, which solidified at a significantly lower growth rate, solidified as primary ferrite and was resistant to cracking.

For a given alloy, when the welding speed results in solidification growth rates close to the critical value, as designated by R_{c1} or R_{c2} in Fig. 11, growth rate fluctuations arising from crystallographic orientation may result in mixed-mode solidification and variable weld solidification cracking susceptibility.

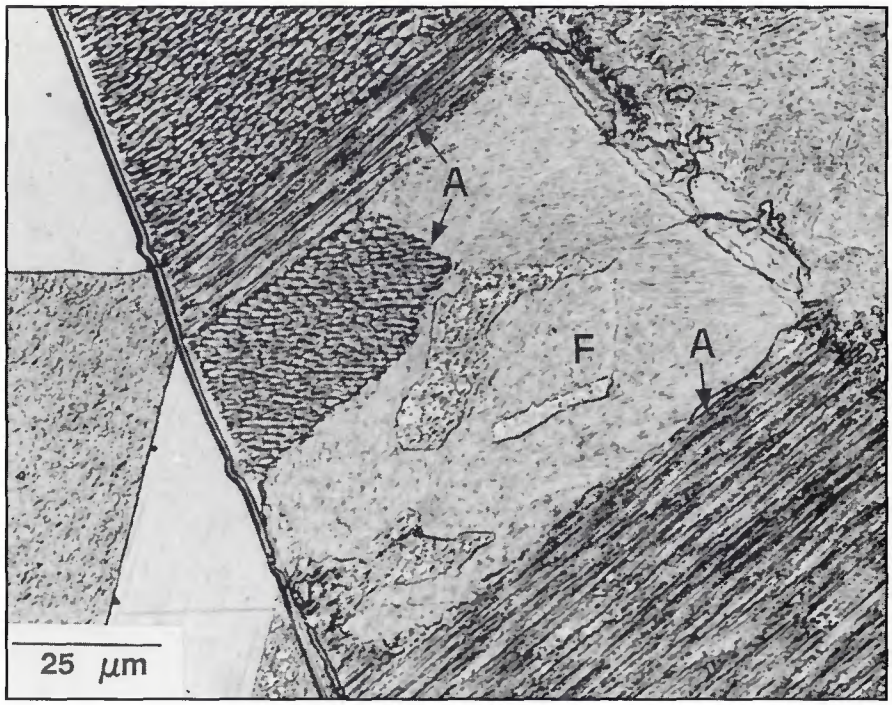

Fig. 12 — Variation in primary solidification as a function of growth orientation in Type 304L (No. 3), 800X.

Nucleation Effects

Epitaxial nucleation from base metal grains at the weld solidification boundary (fusion line) or from a weld metal substrate (at interpulse boundaries) may also influence the solidification behavior. In several of the alloys where solidification occurred predominantly as primary ferrite, some indication of a precursor austenite solidification mode was observed at the nucleation sites. This behavior is illustrated in Fig. 13 for both base metal (*i.e.*, HAZ) and weld metal epitaxy. The region over which austenite solidification occurs was found to be extremely localized with ferrite solidification becoming quickly predominant.

The preferential nucleation of primary austenite relative to ferrite may be due to the presence of an austenitic substrate at the interface. Under normal arc welding conditions, the HAZ in these alloys would transform to ferrite due to the high ferrite potential (Table 4), and primary ferrite would nucleate. During pulsed-laser welding, however, the diffusion-controlled transformation from austenite to ferrite is probably suppressed, preserving the austenitic substrate. In alloys with a sufficiently high Cr_{eq}/Ni_{eq}, the primary phase will shift to ferrite as the growth rate increases away from the epitaxial substrate, as described schematically in Fig. 11 and shown in Fig. 13. At some critical lower Cr_{eq}/Ni_{eq}, the weld will nucleate and solidify as primary austenite.

In summary, microstructural evidence suggests that epitaxial nucleation from an austenitic substrate in pulsed-laser welds occurs preferentially as primary austenite. Once nucleated, the primary phase of solidification depends on the interplay between growth rate and composition, as described in Fig. 11. For a given growth rate, higher Cr_{eq}/Ni_{eq} values favor a transition to primary ferrite solidification, while increased growth rate for a given Cr_{eq}/Ni_{eq} will eventually favor continued solidification as primary austenite. The rapid transition to ferrite solidification may result from the formation of eutectic ferrite during primary austenite solidification that then acts as a nucleation site for ferrite solidification. Similarly, the presence of ferrite in the HAZ at the fusion boundary may serve to nucleate primary ferrite solidification. Neither of these scenarios could be verified as operable during this investigation.

Summary of Microstructural Effects

In an effort to summarize the microstructural aspects resulting from rapid solidification of austenitic stainless steels, the present results and those of other investigators (Refs. 21, 23, 31, 35) have been used to construct a mi-

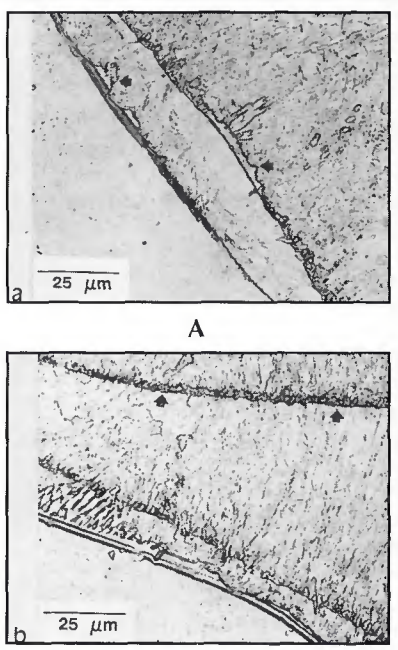

Fig. 13 — Epitaxial nucleation in Type 304L, 800X. A — Base metal epitaxy; B — weld metal epitaxy.

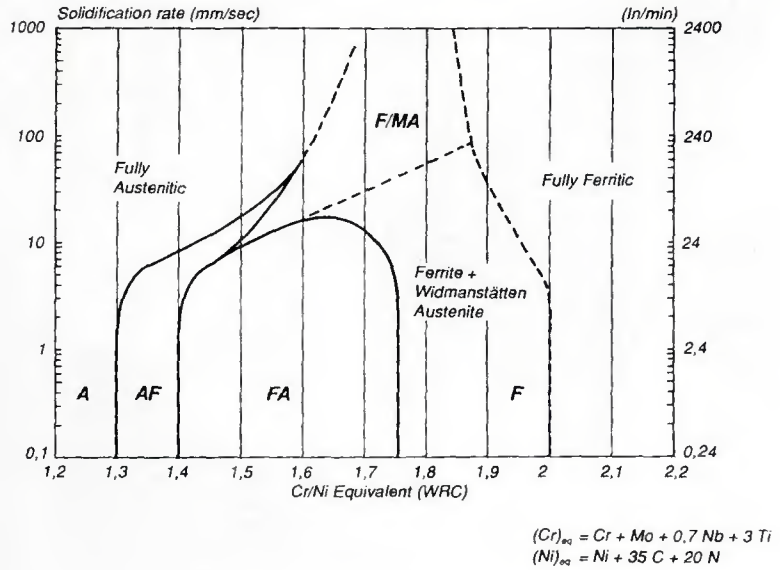

Fig. 14 — Preliminary microstructural map for austenitic stainless steel welds as a function of solidification growth rate, derived in part from (Refs. 21, 23, 31, 35).

crostructural "map" as a function of solidification rate and composition. This map, shown in Fig. 14, represents a preliminary attempt to rationalize the variety of microstructures observed in austenitic stainless steel welds. It is anticipated that slight modifications to this map will be required as additional alloys are evaluated over a wider range of solidification growth rates. In addition, it is not clear that a single map can be used to represent the entire range of 300-series stainless steels. Individual maps may be required for alloys or subgroups of alloys with similar chemical compositions.

Solidification growth rate, as a function of composition, has been chosen to represent the variation in microstructure for several reasons. Most of the pertinent data available in the literature uses a variation in welding speed to produce transitions in the weld microstructure. The welding speed employed could then be used as an upper bound of the solidification rate, as discussed previously. Weld heat input, which is commonly used to describe changes in the microstructure in other systems, appeared to have a secondary effect on microstructural development at high solidification growth rates, as shown in this study and also by the work of David, *et al.* (Ref. 21). It is also recognized that weld cooling rate has a significant influence on microstructure in austenitic stainless steels, although the transition in solidification behavior is primarily a function of growth rate. Since the cooling rate is a product of the solidification growth rate and the temperature gradient in the solid, an increasing growth rate (welding speed) results in increased weld cooling rates assuming the temperature gradient does not change appreciably.

At high welding speeds this is probably a reasonable assumption. Zacharia, *et al.* (Ref. 40), determined that the cooling rate in pulsed-laser welds (Ref. 21) increased by a factor of 16 (0.56 to 8.8 x 10^5°C/s) when the weld travel speed was increased by a factor of 20 (2.12 to 42.33 mm/s) at a constant power level. This predicts a relatively small range of temperature gradient (2.6 to 2.1 10^4°C/mm) over a wide range of solidification growth rates, again assuming that the maximum growth rate equals the welding speed. Thus, as a first approximation, growth rate and cooling rate can be treated equivalently in the rapid solidification region (above 10 mm/s) of Fig. 14. At lower solidification growth rates (welding speeds), weld microstructure is a strong function of composition (Ref. 35) and not so dependent on welding variables. As a result, boundaries between microstructural regions are essentially vertical at low growth rates.

As growth rate increases, microstructural changes resulting from solidification-controlled transitions cause boundary shifts with a positive slope, while changes resulting from diffusion-controlled transitions have a negative slope. Thus, the A/AF boundary shifts to higher Cr_{eq}/Ni_{eq} values at growth rates above approximately 10 mm/s. Conversely, the FA/F boundary shifts to lower Cr_{eq}/Ni_{eq} values in the same range due to a suppression of the solid-state, ferrite-to-austenite transformation. Within the FA region, the diagram can potentially be used to predict the various ferrite morphologies that are dictated by the diffusion-controlled transformation, *i.e.*, vermicular (skeletal) and acicular structures. Eventually, iso-FN lines could be added for estimating weld ferrite content.

Figure 14 can also be used to predict the susceptibility of austenitic stainless steels to solidification cracking when considering both compositional and welding process variables. Weld solidification cracking potential, as described in this investigation, would be highest in the regions designated A and AF. These regions are essentially a projection of the crack-susceptible envelopes predicted by the Suutala and modified Suutala diagrams in Figs. 1 and 3 (for WRC equivalents) over a range of solidification growth rates. Additional experiments over a wide range of composition and solidification growth rates are currently being conducted to better define the crack-susceptible envelopes in Fig. 14 and on the preliminary diagrams shown in Figs. 2 and 3.

While the microstructural map in Fig. 14 represents a reasonable approximation of the metallurgical behavior of austenitic stainless steels over a range of composition, and solidification growth and cooling rate conditions, it should be understood that the absolute definition of the regions defined will require significant additional research.

Conclusions

1) Current predictive diagrams for microstructure and weld solidification cracking susceptibility in austenitic stainless steels are not accurate under the rapid solidification conditions encountered during pulsed-laser welding.

2) Solidification cracking is associated with a shift in weld solidication behavior that occurs under rapid solidification conditions. Solidification as primary austenite was found to be most detrimental.

3) Solidification cracking was found to be primarily a function of composition. Pulsed-laser welding process parameters had only a small influence on cracking over the parametric range examined in this study.

4) A predictive diagram, based on the original Suutala diagram, has been proposed to determine weld solidification cracking susceptibility in austenitic stainless steels under rapid solidification conditions.

5) A solidification model is discussed that relates the transition in primary solidification from ferrite to austenite to dendrite tip undercooling at high solidification growth rates.

6) A preliminary microstructural map

is proposed for austenitic stainless steel welds that takes into account the solidification growth rate.

Acknowledgments

The author would like to thank the Institut de Soudure, Paris, France, for providing partial financial support and a pleasant working environment during the course of this investigation. The author is indebted to Mssrs. G. Pacary and M. Moline, formerly of Institut de Soudure in Metz, for performing the laser welding trials, and to Tom Lienert, graduate research assistant at The Ohio State University for his help in microstructural analysis. Appreciation is extended to W. A. Baeslack, The Ohio State University, for critically reviewing this manuscript and providing a number of helpful suggestions.

References

1. Scherer, R., Riedrich, G., and Hoch, G. 1939. Einfluss eines gahaltes in austenischen chrom-nickel-stahlen auf den kornzerfall. *Archiv. fur das Eisenhuttenwesen,*13:52.

2. Schaeffler, A. L. 1949. Constitution diagram for stainless steel weld metal. *Metal Progress,* 56(11):680.

3. DeLong, W., Ostrom, G., and Szumachowski, E. 1956. Measurement and calculation of ferrite in stainless steel weld metal. *Welding Journal,* 35(11):S26-s.

4. Siewert, T. A., McCowan, C. N., and Olson, D. L. 1988. Ferrite number prediction to 100 FN in stainless steel weld metal. *Welding Journal,* 67(12):289-s.

5. Kotecki, D., and Siewert, T. A. 1992. WRC-1992 constitution diagram for stainless steel weld metals: a modification to the WRC-1988 diagram. *Welding Journal* 71(5):171-s to 178-s.

6. Hull, F. C. 1967. Effect of delta ferrite on hot cracking of stainless steel. *Welding Journal,* 46(9):399-s.

7. Masumoto, I., Tamaki, K., and Kutsuna, M. 1972. Hot cracking of austenitic stainless steel weld metal, *Trans. JWS,* 41(11):1306.

8. Tamura, H. 1972. Weld cracking of austenitic stainless steel. *Jour. Japan Welding Society,* 41(2):127.

9. Arata, J., Matsuda, F. and Katayama, S. 1976. Fundamental investigation on solidification behavior of fully austenitic and duplex microstructure and effect of ferrite on microsegregation. *Trans. JWRI,* 5(2):35.

10. Kujanpaa, V., Suutala, N., Takalo, T., and Moisio, T. 1979. Correlation between solidification cracking and microstructure in austenitic and austenitic-ferritic stainless steel welds. *Welding Research Int.,* 9(2):55.

11. David, S. A., Goodwin, G. M., and Braski, D. N. 1979. Solidification behavior of austenitic stainless steel filler metals. *Welding Journal,* 58(11):330-s.

12. Lippold, J. C. 1982. Weld cracking mechanisms in austenitic stainless steel. *Trends in Welding Research in the U.S.,* pp. 209–247. ASM Conference Proceedings, Materials Park, Ohio.

13. Brooks, J. A., and Thompson, A. W. 1991. Microstructural development and solidification cracking susceptibility of austenitic stainless steel welds. *Int. Met. Reviews,* 36(1):16–44.

14. Lippold, J. C., and Savage, W. F. 1980. Solidification of austenitic stainless steel weldments — Part 2 the effect of alloy composition on ferrite morphology. *Welding Journal,* 59(2):48-s.

15. Suutala, N., Takalo, T., and Moisio, T. 1979. Relationship between solidification and microstructure in austenitic and austenitic-ferritic stainless steel welds. *Met. Trans.,* 10A:512.

16. Katayama, S., Fujimoto, T., and Matsunawa, A. 1985. Correlation among solidification process, microstructure, microsegregation and solidification cracking susceptibility in stainless steel weld metals, Trans. *JWRI,*14(1):1–23.

17. Brooks, J. A., and Lambert, F. J. 1978. The effects of phosphorus, sulfur and ferrite content on weld cracking of Type 309 stainless steel. *Welding Journal,* 57(5):139-s.

18. Arata, Y., Matsuda, F. and Katayama, S. 1977. Solidification crack susceptibility in weld metals of fully austenitic stainless steels — Report 3, effect of ferrite, P, S, C, Si, and Mn on ductility properties of solidification brittleness. *Trans. JWRI,* 6(1):105.

19. Kou, S., and Le, Y. 1982. The effect of quenching on the solidification structure and transformation behavior of stainless steel welds. *Met. Trans.* 13A:1141.

20. Katayama, S., and Matsunawa, A. 1985. Solidification behavior and microstructural characteristics of pulsed and continuous laser welded stainless steels. *Proc. of ICALEO,* pp. 19–25.

21. David, S. A., Vitek, J. M., and Hebble, T. L. 1987. Effect of rapid solidification on stainless steel weld metal microstructures and its implications on the Schaeffler diagram. *Welding Journal,* 66(10):289-s.

22. Nakao, Y., Nishimoto, K., and Zhang, W. 1988. Effects of rapid solidification by laser surface melting on solidification modes and microstructures of stainless steels. *Trans. JWS,* 19:101

23. Elmer, J. W., Allen, S. M., and Eagar, T. W. 1990. The influence of cooling rate on the ferrite content of stainless steel alloys. *Recent Trends in Welding Science and Technology,* pp. 165–170. Eds. S. A. David and J. M. Vitek. ASM International, Materials Park, Ohio.

24. Elmer, J. W., Eagar, T. W., and Allen, S. M. 1990. Single phase solidification during rapid resolidification of stainless steel alloys. *Weldability of Materials,* eds. R. A. Patterson and K. W. Mahin, ASM International, Materials Park, Ohio, pp. 143–150.

25. Brooks, J. A., and Baskes, M. I. 1990. Microsegregation modeling and transformation in rapidly solidified austenitic stainless steel welds, *Recent Trends in Welding Science and Technology,* Eds. S. A. David and J. M. Vitek. ASM International, Materials Park, Ohio, pp. 153–158.

26. Varol, I., Baeslack, W. A., and Lippold, J. C. 1989. Characterization of weld solidification cracking in a duplex stainless steel, *Metallography,* 23:1–19

27. Pease, G. R. 1957. The practical welding metallurgy of nickel and high-nickel alloys, *Welding Journal,* 36(7):330-s.

28. Kelly, T. 1990. Investigation of elemental effects on the weldability of cast nickel-base superalloys, *Recent Trends in Welding Science and Technology,* pp. 623–627. Eds. S. A. David and J. M. Vitek. ASM International, Materials Park, Ohio.

29. Lippold, J. C., Noble, D. N., and Rundell, G. 1990. The weldability of high-C, high-Si stainless steels. Unpublished work.

30. Borland, J. C. 1961. Suggested explanation of hot cracking in mild and low alloy steel welds, *British Welding Journal,* 8:526–540.

31. Lippold, J. C. 1985. Centerline cracking in deep penetration electron beam welds in Type 304L stainless steel. *Welding Journal* 64(5):127-s to 136-s.

32. Vitek, J. M, Dasgupta, A., and David, S. A. 1983. Microstructural modification of austenitic stainless steels by rapid solidification. *Met. Trans.* 14A:1833–1841.

33. Easterling, K. 1983. *Introduction to the Physical Metallurgy of Welding.* Butterworths and Co., Ltd., p. 57.

34. Kurz, W., and Fisher, D. J. 1984. *Fundamentals of Solidification.* Tech Trans Publication, Switzerland, p. 27.

35. Suutala, N. 1982. Effect of solidification conditions on the solidification mode in austenitic stainless steels. *Acta Universitatis Ouluensis,* Series C, Technica No. 23, Metallurgica No. 3, University of Oulu, Oulu, Finland.

36. Burden, M. H., and Hunt, J. D. 1974. *Journal of Crystal Growth* 22:99–108, 109–116.

37. Kurz, W., and Fisher, D. J. 1981. Dendrite growth at the limit of stability: tip radius and spacing. *Acta Met.* 29:11–20.

38. Fredriksson, H. 1979. *Solidification and Casting of Metals,* The Metals Society, U. K.

39. Okamoto, T., Kishitake, K., and Murakami, K., 1981. *Trans. JISI* 21:641.

40. Zacharia, T., David, S. A., Vitek, J. M., and Debroy, T. 1989. Heat transfer during Nd:YAG welding and its effect on solidification structure of austenitic stainless steels, *Met. Trans.* 20A:957–967.